Evaluation of a Concerted versus Sequential Oxygen Activation Mechanism in α-Ketoglutarate Dependent Nonheme Ferrous Enzymes

Serra Goudarzi,[†,⋆] Shyam R. Iyer,[†,⋆] Jeffrey T. Babicz Jr.,[†] James J. Yan,[†] Günther H. J. Peters,[‡] Hans E. M. Christensen,[‡] Britt Hedman,[¶] Keith O. Hodgson,[†,¶] Edward I. Solomon[†,¶]

† *Department of Chemistry, Stanford University, Stanford, California 94305, United States*

‡ *Department of Chemistry, Technical University of Denmark, Kgs. Lyngby, Denmark*

¶ *Stanford Synchrotron Radiation Light Source, SLAC National Accelerator Laboratory, Stanford University, Menlo Park, California 94025, United States*

⋆ *S.G. and S.R.I. contributed equally to this work.*

www.pnas.org/cgi/doi/10.1073/pnas.1922484117

1 Materials and Methods

1.1 DAOCS Expression and Purification

All chemicals used were of analytical grade, and all solutions were prepared using water from an 18.2 MΩ·cm Milli-Q synthesis A10 Q-Gard system which was filtered through a 0.22 μm filter. Protein purification was performed on an ÄKTA Start utilizing GE Healthcare column variants: Q Sepharose HP 26/10 (ion exchange) and a Superdex 75 26/60 (gel filtration). Protein solutions were concentrated using an Amicon ultrafiltration cell with an Ultracell PL-3 membrane. Protein concentrations were determined by measuring the absorbance at 280 nm on an ND-1000 NanoDrop Spectrophotometer from Saveen Werner.

DAOCS cDNA optimized for expression in *E. coli* was obtained from GenScript, and the protein was expressed from the pET26 expression vector in *E. coli* BL21(DE3) (Novagen) cells. Glycerol stock solution of HC2516 on LB/30kan (30 μg kanamycin/mL LB agar) was striped on the agar and incubated at 37 °C overnight. A single colony was chosen to inoculate in 50 mL LB/30kan (30 μg kanamycin/mL LB medium) and incubated at 37 °C with shaking (250 rpm on Inova incubator) for approximately 4 hours until the OD_{600} of 0.6-1.0 was reached. The culture was stored at 4 °C overnight. The culture was then transferred to a 50 mL sterile plastic tube and centrifuged at 3000 rpm for 10 min at 4 °C. The supernatant was decanted off, and the pellet was resuspended in 50 ml LB/30kan. Each of the 6x6.5 mL was transferred to 650 mL LB/30kan and incubated at 30 °C with shaking (250 rpm on Inova incubator). The temperature of the incubator was reduced to 20 °C once the OD_{600} reached 0.30-0.39. Once the OD_{600} reached 0.5-0.6, 0.2 M, ammonium ferrosulfate and Isopropyl β-D-1-thiogalactopyranoside (IPTG) were added to a final concentration of 0.2 mM and 0.1 mM, respectively. The incubation was continued overnight (16-18 hours). Each culture was then transferred to a Beckman centrifuge tube and centrifuged at 3900 rpm for 15 min at 4 °C. The supernatant was decanted off, and the cells were transferred to a 50 ml non-sterile plastic tube with 25 ml of 20 mM BIS-TRIS propane/H_2SO_4, pH 6.8. The samples were centrifuged at 3900 rpm for 15 min at 4 °C, the supernatants were discarded and the cells were stored at -80 °C.

E. coli cells from 2x650 mL cultures were defrosted in ice water, and each cell culture was resuspended in buffer containing 20 mM BIS-TRIS propane/H_2SO_4, pH 6.8 (buffer A). The resuspended cell cultures were lysed by sonication for 3x30 seconds using a Satorius Labsonic at 80% amplitude, while kept in ice water. The lysed samples were centrifuged for 2x20 min. at 13,000 rpm at 4 °C. The supernatants were immediately decanted off and filtered through 0.45 μm syringe filter. The cell extract is diluted with approximately 20 mL of Milli Q water until the conductivity is below 2.2 mS/cm which equals the conductivity of the buffer A. The cell extract was loaded on an anion exchange (IEX) Q Sepharose HP 26/10 column, using an external pump and a loading flow rate of 8 mL/min. The column was washed with IEX buffer A until a steady plateau in the 280 nm absorbance was achieved, in order to remove any weakly bound contaminants. Elution of the protein was done by applying IEX buffer B (20mM BIS-TRIS propane/H_2SO_4 + 0.33M ammonium sulfate, pH 6.8) with a gradient of 5% buffer B/CV. The flowrate was 8 mL/min. Fractions corresponding to the major peak eluding at about 14% buffer B were collected ($\sim$40 mL), and the collected solution was up-concentrated using an Amicon cell ($\sim$5 mL). The Amicon cell was rinsed with $\sim$2 mL of the gel filtration buffer (20 mM HEPES/NaOH + 100 mM ammonium sulfate, pH 6.8). The solution was filtered through a 0.45 μm filter prior to loading on a gel filtration column, Superdex 75 26/60, with a flow-rate of 2.5 mL/min that was also used for elution of the protein. Fractions corresponding to the major peak eluding at about 160 mL are collected. The concentration of protein was determined on a NanoDrop spectrophotometer using the extinction coefficient for DAOCS of 26275 $M^{-1} \cdot cm^{-1}$ and MW of 34555.7 g/mol. The purified protein was distributed into aliquots, frozen in liquid nitrogen and stored at -80 °C.

1.2 Sample Preparation

Samples for spectroscopy were prepared under an inert atmosphere inside an N_2-purged wet box. DAOCS was made anaerobic by purging under a nitrogen atmosphere on a Schlenk line at 0° C for approximately 1 hour. Ferrous ammonium sulfate, αKG and penicillin G were added from anaerobic stock solutions in deuterated HEPES buffer for CD and MCD samples and in HEPES buffer for Mössbauer, XAS, SF-Abs and EPR samples. CD was used to monitor cofactor and substrate binding, where each was added until no further spectral change was observed before preparation of MCD samples. For preparation of MCD cells, samples were saturated with deuterated sucrose for a glassing agent. CD spectra were taken without and with sucrose to ensure that the glassing agent did not perturb the Fe^{II} site.

1.3 Spectroscopic Methods

Absorption spectra were measured with an Agilent HP8453 diode array spectrophotometer at room temperature. Near-IR (600-2000 nm) CD and MCD spectra were recorded with a Jasco J-730 spectropolarimeter with a liquid N_2-cooled InSb detector (Teledyne Judson Technologies) and an Oxford Instruments SM-4000-7T superconducting magnet. UV-Vis (300-900 nm) CD and MCD data were recorded with a Jasco J-810D spectropolarimeter with an extended S-20 photomultiplier tube and an Oxford Instruments SM-4000-7T superconducting magnet. MCD spectra were corrected for baseline and CD features by subtracting a 0 T scan at each temperature. The sample temperature was measured using a calibrated Cernox resistor (Lakeshore Cryogenics, calibrated 1.5-300 K) that was inserted into the MCD cell. VTVH MCD data were normalized to the maximum intensity over all isotherms for a given wavelength. X-band EPR spectra were taken on a Bruker EMX spectrometer with a Bruker ER 041XG/ER microwave bridge and 4116 DM cavity. Spectra were collected at 77 K or at 5 K using an Oxford ITC503 temperature controller with an ESR 900 continuous flow cryostat. Mössbauer spectra were collected at 6 K or 50 K using a See Co. W302 resonant gamma ray spectrometer using a 1.85-GBq ^{57}Co source (Be window, Rh matrix) and with zero external magnetic field. All isomer shifts are given relative to Fe metal at room temperature. Spectra were analyzed using WMoss software package (See Co.).

1.4 X-ray Absorption Experiments and Data Analysis

XAS cells (2 mm x 10 mm pinhole-type Delrin cells wrapped with Kapton tape) were loaded with protein samples and then frozen under liquid nitrogen. The samples were oriented at 45° to the incident X-ray beam and maintained at 10 K using an Oxford Instruments CF1208 continuous flow liquid helium cryostat. XAS data were collected at beam lines 7-3[1] and 9-3[2] at SSRL under ring operating conditions of 500 mA over an energy range of 6785-7876 eV (k = 14 Å^{-1}). Fluorescence data were collected at 90° to the incident beam using a solid-state 30- or 100-element Ge detector array with Soller slits and a six-wavelength Mn filter aligned between the sample and the Soller slit to improve the Fe Kα fluorescence signal intensity relative to that of the scattered beam.[3] An internal calibration was utilized with the first inflection point of an Fe foil set to 7111.2 eV.[4]During measurement, the data in the Fe K-edge, K pre-edge, and EXAFS regions were continuously monitored to ensure sample integrity by comparing each individual scan to ones taken previously. No photodamage was observed in the samples.

Data reduction, background subtraction, and normalization were performed according to established methods[5,6,7] using the program PySpline[8] with the data normalized to a value of 1.0 at the post-edge region. The spline function through the EXAFS region was chosen to minimize any residual low-frequency background but not reduce the EXAFS amplitude, as monitored by the Fourier transform intensity. For pre-edge and edge analysis, all data sets were truncated to k = 9.5 Å^{-1} and renormalized using a second-order post-edge polynomial background and a two segment (three knot) spline for comparison between data sets and to past reference compounds.[9] Normalization of the EXAFS data was accomplished using a third-order postedge polynomial background fit over the full data range (k = 14 Å^{-1}) and a three-segment (four-knot) spline for resting DAOCS, penG, and αKG, and a four-segment (five-knot) spline for αKG/penG.

Iron K pre-edge features were modeled with a pseudo-Voigt line shape in a 50 : 50 ratio of Lorentzian : Gaussian functions using the fitting program EDG_FIT[10] as part of the program suite EXAFSPAK.[11] The energy position, full width at half-maximum (fwhm), and peak intensity were all allowed to float throughout the fitting process. A function modeling the background was empirically chosen to give the best fit, floated with all variables, and then varied with different fwhm (up to ±0.5 from float) to establish confidence limits on pre-edge intensity. In all cases, an acceptable fit reasonably matched both the pre-edge data as well as those of its second derivative. Fits with backgrounds were acquired over the energy ranges of 7106-7116, 7106-7117, and 7106-7118 eV to provide twenty pre-edge fits. These were then averaged to give the final pre-edge energy and intensity values.

EXAFS signals were calculated using FEFF (version 7.0), and the data were fit using the program OPT[12] as part of EXAFSPAK. In all fits the bond lengths (R) and bond variances (σ^2) were allowed to vary. The threshold energy ($k = 0, E_0$) was also allowed to vary but was constrained as a common variable (ΔE_0) for all fit paths in a given data set. The amplitude reduction factors (S_0^2) were fixed to a value of 1.0, and the coordination numbers (CN) were varied systematically based on a structural model to achieve the best fit to the EXAFS data. The best choice of all available FEFF paths and the goodness of the overall fit were optimized based on a combination of weighted F-factor (F)[13] as well as visual fit to the EXAFS data and their Fourier transform. On the basis of studies of complexes of known structures, the uncertainties in final distances are within 0.02 Å.[14] The EXAFS data were fit using crystal structures 1RXF,[15] 1UOF,[16] and 1UOB[16] as initial models for Fe^{II}-DAOCS, (Fe^{II}/penG)-DAOCS, and (Fe^{II}/αKG)-DAOCS/(Fe^{II}/αKG/penG)-DAOCS, respectively.

1.5 Stopped-Flow Absorption Experiments and Kinetic Simulations

Stopped-flow absorption experiments were carried out at 4° C using an Applied Photophysics SX19 stopped-flow spectrophotometer using a 1 cm path length equipped with a photodiode array inside a purge glove box in an Ar atmosphere. O_2-free stock solutions of (Fe^{II}/αKG)-DAOCS and (Fe^{II}/αKG/penG)-DAOCS were prepared as described above. The DAOCS solutions were mixed with an equal volume of either O_2-free buffer or buffer that had been saturated with O_2 at 0° C then allowed to reach equilibrium at 5° C before mixing for excess O_2 experiments. For one equivalent or substoichiometric O_2 experiments, the saturated O_2 solution was diluted, then allowed to reach equilibrium at 5° C before mixing. Kinetic simulations were performed with COPASI.[17]

1.6 Computational Methods

The penicillin G molecule was created using GaussView and geometry optimized. All other structures were created from this output and then geometry optimized. Calculations were performed using the Gaussian 09 software package, revision D.01.[18] The unrestricted BP86 functional[19] with 10% Hartree-Fock exchange under tight convergence criteria was used for all calculations. The 6-311G* basis set was used. Solvation effects were included using a polarized continuum model with a dielectric constant $\epsilon = 4.0$ to model the protein environment.[20] Time-dependent density functional theory (TD-DFT) calculations were performed using the CAM-B3LYP functional.[21]

2 Supplementary Information

2.1 Interaction of αKG and penG with Fe^{II}/DAOCS: Availability of a five-coordinate Fe^{II}/αKG site

2.1.1 Circular Dichroism (CD) Spectroscopy

CD spectroscopy was used to confirm the lack of interaction of sucrose, which is used as an glassing agent, with the active site.

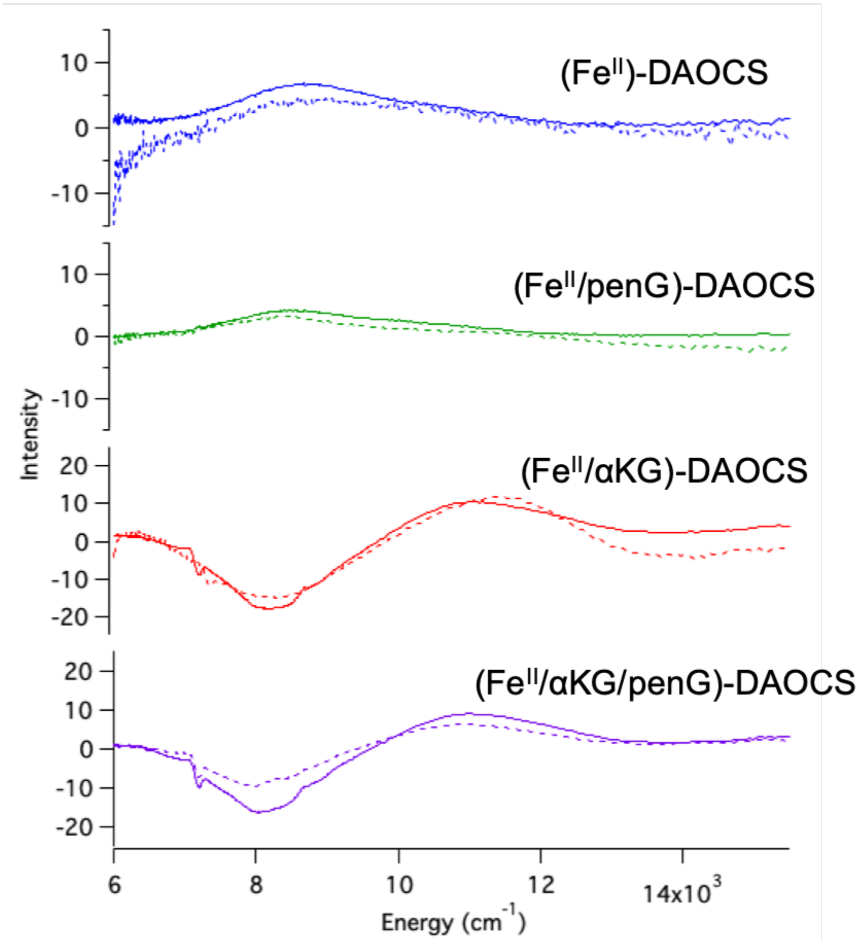

Figure S1: Comparison of the CD spectra for (Fe^{II})- (blue), (Fe^{II}/penG)- (green), (Fe^{II}/αKG)- (red) and (Fe^{II}/αKG/penG)-DAOCS (green) in the presence (dashed) and absence (solid) of added sucrose. These results demonstrate that sucrose, used as a glassing agent, does not perturb the active site.

2.1.2 VTVH MCD to define Fe^{II} dπ orbital splittings[22,23]

VTVH MCD data can be used to determine the ground state splitting of Fe^{II} sites. MCD intensity increases with increasing field and decreasing temperature. A plot of MCD intensity at a single energy of an MCD feature against βH/2kT results in a set of saturation magnetization isotherms that overlay for a Kramers S = 1/2 system. For a non-Kramers system, including the S = 2 integer spin systems studied here, these isotherms show nesting behavior. In a system with negative zero-field splitting (ZFS), the nesting behavior is due to the field dependent mixing of the M$_S$ = +2 and M$_S$ = -2 wavefunctions, and the degree of mixing is proportional to the magnitude of δ, the splitting of these components in zero field. VTVH isotherms are fit to this non-Kramers doublet model to derive the ground state spin-Hamiltonian parameters ($g_{\|}$ and δ), that in turn determine the axial and rhombic splitting (Δ = d$_{xz,yz}$ - d$_{xy}$ and $|V|$ = d$_{xz}$ - d$_{yz}$) of the dπ orbitals. For a positive zero-field split system (D > 0), the M$_S$ = 0 sublevel is lowest with the M$_S$ = ±1 doublet at higher energy. When the field is perpendicular to the z-axis of the ZFS tensor, the M$_S$ = 0 interacts with one component of the M$_S$ = ±1 doublet in a field dependent manner to also give nesting behavior that can again be fit to define the ZFS parameters (D and E) and thus the splitting of the dπ orbitals (Δ and $|V|$). In this way, the sign and magnitude of the dπ orbital splittings can be determined.

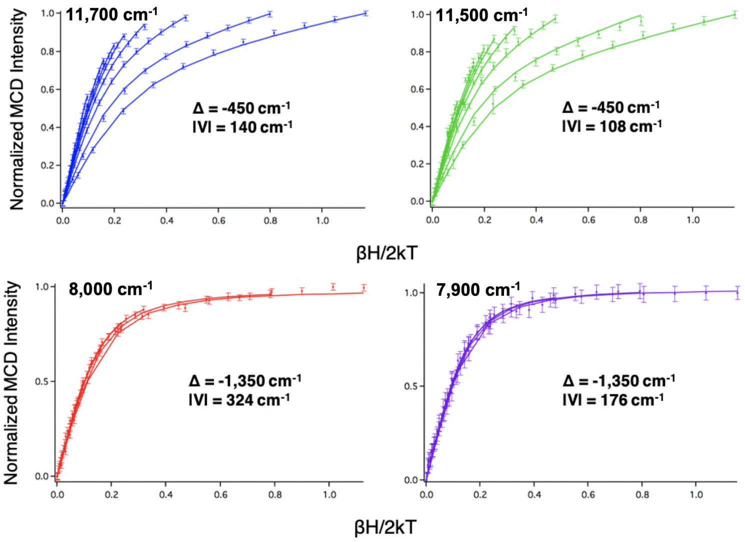

Figure S2: *Top Isotherms.* Saturation magnetization data and best fits for Fe^{II}-DAOCS (blue) and (Fe^{II}/penG)-DAOCS (green). The axial splittings of the dπ orbitals (Δ = $d_{xz,yz}$ - d_{xy}) for both Fe^{II}-DAOCS and (Fe^{II}/penG)-DAOCS are consistent with distorted 6C sites, supporting the assignment made from the MCD spectra (Figure 1) based on excited state splittings. The difference in the rhombic splittings ($|V| = d_{xz}$ - d_{yz}) indicates that substrate binding has perturbed the 6C Fe^{II} ground state. *Bottom Isotherms.* Saturation magnetization data and best fits for (Fe^{II}/αKG)-DAOCS (red) and (Fe^{II}/αKG/penG)-DAOCS (purple). The axial splittings of the dπ orbitals (Δ) for both (Fe^{II}/αKG)-DAOCS and (Fe^{II}/αKG/penG)-DAOCS are increased relative to the sites without αKG bound. Although these splittings are large for 6C sites, increased Δ values have been observed for the αKG-bound 6C sites of two other NHFe^{II} enzymes, FIH and CS2.[24,25] These large splittings are due to π-backbonding of the Fe^{II} dπ into the π^* orbital of the αKG ligand. The difference in the rhombic splittings ($|V|$) indicates that substrate binding to the αKG-bound site has perturbed the Fe^{II} ground state.

2.1.3 Evidence for bidentate αKG binding to Fe$^{\text{II}}$(DAOCS)

When αKG interacts with an Fe$^{\text{II}}$ active site, a broad absorption feature near 520 nm grows in, which is a dπ to π^* metal-to-ligand charge transfer (MLCT) indicative of bidentate binding to the metal center[25].

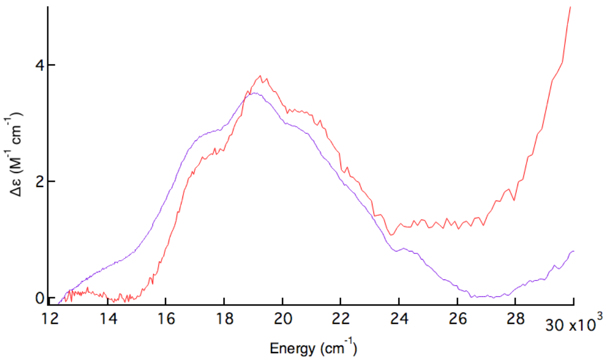

Figure S3: MCD spectra collected at +7 T and 5 K in the UV-Vis region for (Fe$^{\text{II}}$/αKG)-DAOCS (red) and (Fe$^{\text{II}}$/αKG/penG)-DAOCS (purple). This broad feature is an Fe$^{\text{II}}$-to-αKG charge transfer transition and indicates bidentate binding of the αKG cofactor[25].

2.1.4 Deviation from the Sum Rule in Fe$^{\text{II}}$ MCD Spectroscopy

The majority of ferrous systems studied show all MCD transitions with positive intensity, arising from spin-orbit coupling (SOC) between the components of the ^{5}T$_2$ ground state (d_{xy}, d_{xz} and d_{yz} orbitals). A negatively signed transition requires SOC between the excited state components (extra electron in d_{z^2} and $d_{x^2-y^2}$ orbitals). There is no matrix element of the orbital angular momentum (L) to couple these. To provide a mechanism for SOC between the excited state sublevels, one component of the t$_2$ must mix into a component of the e set.[26] In 6C geometries, the e set is high in energy relative to the t$_2$ and there is not significant mixing. In 5C geometries, one component of the e set is lowered in energy and can mix with a component of the t$_2$ set to enable SOC between the two components of the excited state to produce opposite signed bands thus a negative transition, as observed in the MCD spectra of (Fe$^{\text{II}}$/αKG)-DAOCS and (Fe$^{\text{II}}$/αKG/penG)-DAOCS.[26]

2.1.5 Mössbauer Evidence for αKG and penG binding to Fe^{II}(DAOCS)

Mössbauer spectra of (Fe^{II}/αKG)-DAOCS (Fig. S4, *Top*) and (Fe^{II}/αKG/penG)-DAOCS (Fig. S4, *Bottom*) show that substrate binding changes the ratio of the two quadrupole doublets, increasing the doublet with the larger ΔE_Q (blue curve in Fig. S4 and Table S1) that is correlated to a 5C site (Main text and XAS [below]).

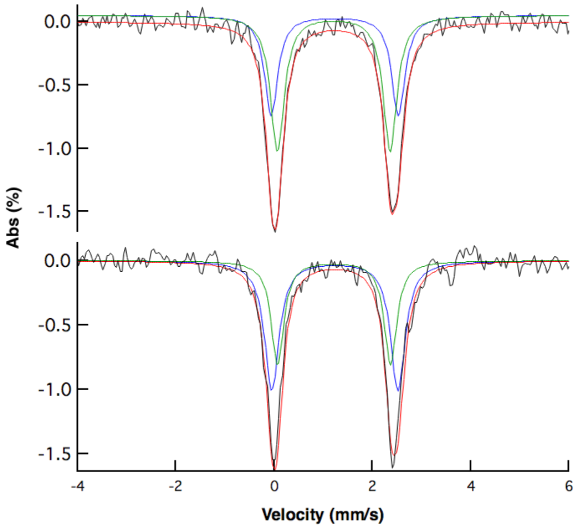

Figure S4: Mössbauer spectra (black) collected at 0 T and 6 K with simulations in red for (Fe^{II}/αKG)-DAOCS (top) and (Fe^{II}/αKG/penG)-DAOCS (bottom). The (Fe^{II}/αKG)-DAOCS spectrum is fit to two species (also observed in MCD spectrum, Fig. 1 [red]), both consistent with high-spin Fe^{II} sites.[27] In this spectrum, species 1 (green) accounts for 54% and species 2 (blue) accounts for 46% of the total Fe. In the spectrum for (Fe^{II}/αKG/penG)-DAOCS, the same two species are present but their quantities have shifted such that species 1 accounts for 41% and species 2 accounts for 59% of the total Fe in solution.

Sample	Species	δ (mm/s)	ΔE_Q (mm/s)	Percentage (%)
Fe^{II}/αKG	1	1.22	2.17	54
	2	1.24	2.47	46
Fe^{II}/αKG/penG	1	1.22	2.17	41
	2	1.24	2.47	59

Table S1: Mössbauer parameters for the two species in (Fe^{II}/αKG)- and (Fe^{II}/αKG/penG)-DAOCS.

2.1.6 X-ray Absorption Spectroscopic Evidence of a 5C (Fe^{II}/αKG)-DAOCS site

XAS was performed on (Fe^{II})-DAOCS (blue), (Fe^{II}/αKG)-DAOCS (red), (Fe^{II}/penG)-DAOCS (green) and (Fe^{II}/αKG/penG)-DAOCS (purple) samples. These spectra have been analyzed in terms of the overall trends in this series going from (Fe^{II})-DAOCS resting site to the ternary (Fe^{II}/αKG/penG)-DAOCS site.

Analysis of the Pre-edge Intensity The Fe K-pre-edge is a 1s-to-3d transition is formally electric dipole forbidden and thus weak in intensity. However, in low symmetry protein environments, 4p mixing into the metal 3d orbitals increases the pre-edge intensity through mixing with the electric dipole allowed 1s-to-4p transition. This mixing is greater for 5C than for 6C ferrous sites, thus making the pre-edge region a probe for coordination number. (Fe^{II})-DAOCS (blue) has the smallest intensity while the (Fe^{II}/αKG/penG)-DAOCS ternary sample has the highest intensity (Fig. S5 and Table S2), which correlates to ternary complex have a higher percentage of a 5C component.

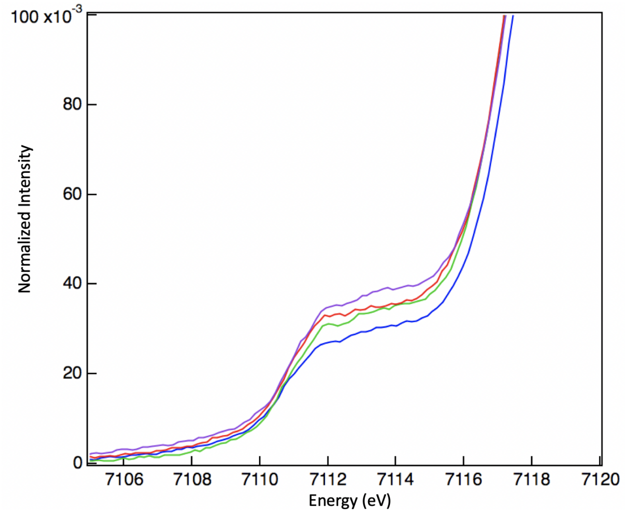

Figure S5: Pre-edge XAS spectra for (Fe^{II})-DAOCS (blue), (Fe^{II}/penG)-DAOCS (green), (Fe^{II}/αKG)-DAOCS (red) and (Fe^{II}/αKG/penG)-DAOCS (purple).

Sample	Intensities
(Fe^{II})-DAOCS	8.2 ± 0.6
(Fe^{II}/αKG)-DAOCS	9.0 ± 0.7
(Fe^{II}/penG)-DAOCS	9.4 ± 2.1
(Fe^{II}/αKG/penG)-DAOCS	10.2 ± 4.2

Table S2: Tabulated pre-edge XAS integrated intensities (background subtracted) for (Fe^{II})-DAOCS (blue), (Fe^{II}/penG)-DAOCS (green), (Fe^{II}/αKG)-DAOCS (red) and (Fe^{II}/αKG/penG)-DAOCS (purple).

Analysis of the White line Peak and Shape Resonance Dip The white line and shape resonance features are sensitive to coordination environment around the iron center. Fe^{II}-DAOCS (blue) has the highest intensity in the white line peak and the lowest intensity in the shape resonance dip (blue arrows) while (Fe^{II}/αKG/penG)-DAOCS has the lowest white line intensity and the highest intensity at the dip (purple arrows). These intensity differences are qualitatively similar to those observed for TyrH, where the active site converts from 6C to 5C upon binding both substrate and cofactor.[28] Thus, this trend shows that the αKG- and αKG/penG-bound Fe^{II}(DAOCS) sites have higher percentages of a 5C component.

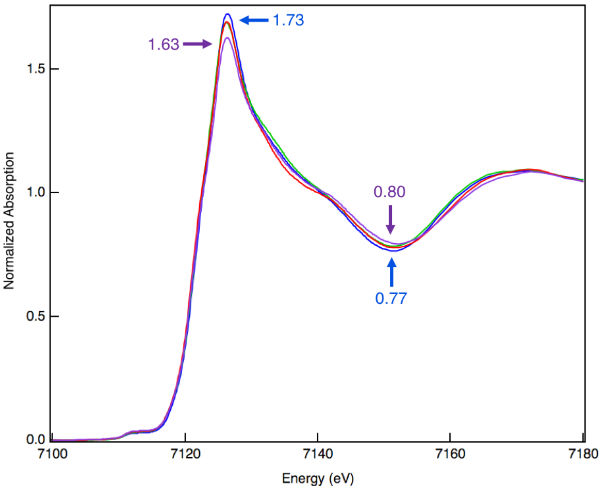

Figure S6: K-edge X-ray Absorption Near Edge Structure spectra for (Fe^{II})-DAOCS (blue), (Fe^{II}/penG))-DAOCS (green), (Fe^{II}/αKG)-DAOCS (red) and (Fe^{II}/αKG/penG)-DAOCS (purple). The blue arrows correspond to the spectrum of (Fe^{II})-DAOCS, while the purple arrows correspond to the spectrum of (Fe^{II}/αKG/penG)-DAOCS.

Extended X-ray Absorption Fine Structure (EXAFS) EXAFS probes the local environment around the Fe^{II} center. In Fig. S6, going from (Fe^{II})-DAOCS (blue) to (Fe^{II}/αKG/penG)-DAOCS (purple), there is a decrease in the EXAFS amplitude (Fig. S7A) and in the intensity of the main fourier transformed peak (Fig. S7B). For (Fe^{II})-DAOCS, the 6C fit has significantly lower error than the 5C fit (Table S3). For the other samples, there is no significant difference in the error or bond lengths for a 6C fit compared to a 5C fit (Tables S3-S7). In going from (Fe^{II})-DAOCS to (Fe^{II}/αKG/penG)-DAOCS, there is a decrease in the first shell bond length from 2.14 to 2.11 Å. Additionally, there is an increase in the first-shell Debye-Waller factor, from 627 in (Fe^{II})-DAOCS to 932 for the 6C fit in (Fe^{II}/αKG/penG)-DAOCS, which indicates increasing disorder in the first shell. The decrease in bond length and increase in Debye-Waller factor reflect a 6C/5C mixture in (Fe^{II}/αKG/penG)-DAOCS. From the combination of XANES and EXAFS data, (Fe^{II})-DAOCS is 6C and then gains a significant amount of 5C component upon binding of both αKG and penG.

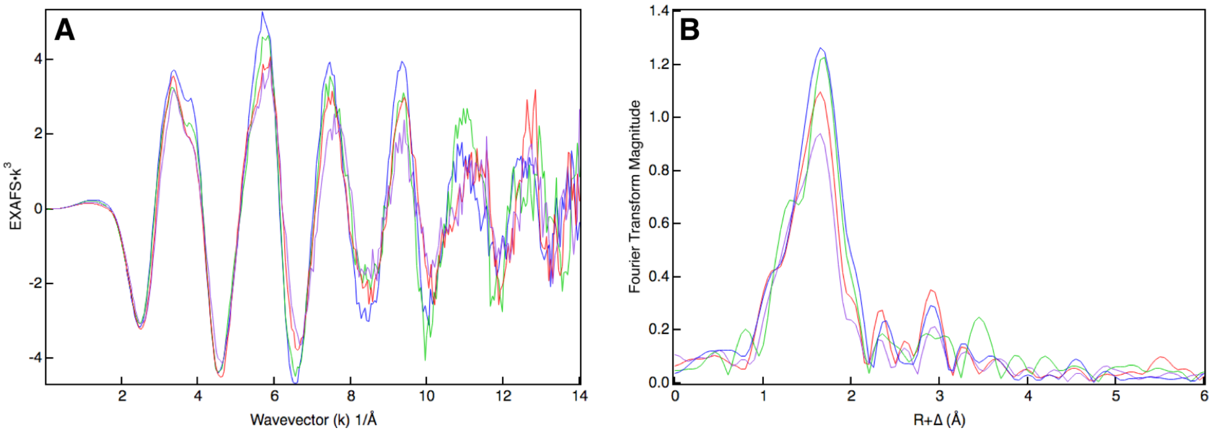

Figure S7: (A) k^3-weighted EXAFS data and (B) Fourier transformed data for Fe^{II}-DAOCS (blue), (Fe^{II}/penG)-DAOCS (green), (Fe^{II}/αKG)-DAOCS (red) and (Fe^{II}/αKG/penG)-DAOCS (purple). As seen in the data, there is a decrease in the EXAFS amplitude and the intensity of the main Fourier Transform peak in going from Fe^{II}-DAOCS (blue) to (Fe^{II}/αKG/penG)-DAOCS (purple). This corresponds to a decrease in the first-shell bond length and increase in σ^2 (Tables S2-S5), which is consistent with an increased 5C contribution.

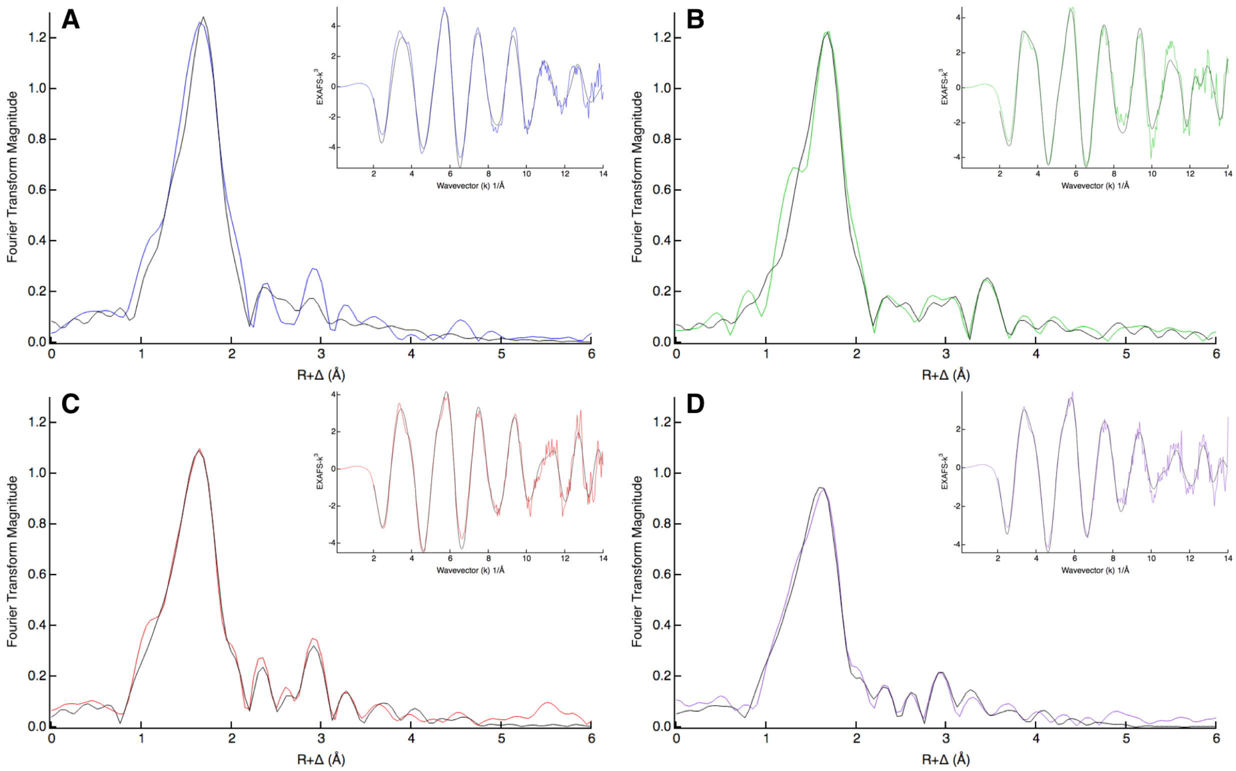

Figure S8: Fourier transformed EXAFS data for (A) Fe^{II}-DAOCS (B) (Fe^{II}/penG)-DAOCS (C) (Fe^{II}/αKG)-DAOCS and (D) (Fe^{II}/αKG/penG)-DAOCS with best fits. Fit parameters listed in Tables S2-S5.

	6C			5C		
	R (Å)	σ^2 (Å^2)	Error	R (Å)	σ^2 (Å^2)	Error
Fe^{II}	**2.14**	**627**	**20.94**	**2.14**	**514**	**23.63**
Fe^{II}/penG	**2.13**	**645**	**23.81**	**2.13**	**518**	**24.86**
Fe^{II}/αKG	**2.12**	**750**	**19.89**	**2.12**	**613**	**20.25**
Fe^{II}/αKG/penG	**2.11**	**932**	**20.43**	**2.11**	**771**	**20.89**

Table S3: First shell EXAFS fits for (Fe^{II})-DAOCS, (Fe^{II}/penG)-DAOCS, (Fe^{II}/αKG)-DAOCS and (Fe^{II}/αKG/penG)-DAOCS using a 6C or 5C model. The uncertainty in EXAFS bond distances is ± 0.02 Å. σ^2 values are multiplied by 10^5. The error value is the weight F-factor given by the statistical F test used to evaluate EXAFS fits.[29] Full parameters for the 6C fits are given in Tables S4-S7. Note the decreased bond lengths and increased σ^2 values in (Fe^{II}/αKG)-DAOCS and (Fe^{II}/αKG/penG)-DAOCS forms.

Component	N	R(Å)	σ^2 (Å^2)
Fe-O/N	6	2.14	627
Fe-C	5	3.14	848
Fe-N	3	4.11	722
C-N MS	2	4.29	265
C-C MS	8	4.48	932
		E_0 = -5.64	
		Error = 20.94	

Table S4: Full fit parameters for Fe^{II}-DAOCS. σ^2 values are multiplied by 10^5. E_0 is the energy shift from 7130 eV to give the experimental ionization energy of the 1s electron. The error value is the weighted F-factor given by the statistical F test used to evaluate EXAFS fits. Error is given by $\Sigma[(\chi_{obsd} - \chi_{calc})^2 k^6]/\Sigma[(\chi_{obsd})^2 k^6]$. MS = multiple scattering. The S_0^2 factor was set at 1.

Component	N	R(Å)	σ^2 (Å^2)
Fe-O/N	6	2.13	645
Fe-C	3	3.11	518
Fe-C	2	3.50	121
C-C MS	6	4.00	672
Fe-C	3	4.24	197
C-N MS	8	4.40	335
C-O MS	8	5.00	751
		E_0 = -5.81	
		Error = 23.81	

Table S5: Full fit parameters for (Fe$^{\mathrm{II}}$/penG)-DAOCS. σ^2 values are multiplied by 10^5. E_0 is the energy shift from 7130 eV to give the experimental ionization energy of the 1s electron. The error value is the weighted F-factor given by the statistical F test used to evaluate EXAFS fits. Error is given by $\Sigma[(\chi_{obsd} - \chi_{calc})^2 k^6]/\Sigma[(\chi_{obsd})^2 k^6]$. MS = multiple scattering. The S_0^2 factor was set at 1.

Component	N	R(Å)	σ^2 (Å^2)
Fe-O/N	6	2.12	750
Fe-C	3	2.96	158
Fe-C	4	3.12	122
C-O MS	10	3.21	936
C-N MS	6	4.29	926
C-O MS	4	4.43	739
Fe-N	2	5.00	583
		E_0 = -6.39	
		Error = 19.89	

Table S6: Full fit parameters for (Fe$^{\mathrm{II}}$/αKG)-DAOCS. σ^2 values are multiplied by 10^5. E_0 is the energy shift from 7130 eV to give the experimental ionization energy of the 1s electron. The error value is the weighted F-factor given by the statistical F test used to evaluate EXAFS fits. Error is given by $\Sigma[(\chi_{obsd} - \chi_{calc})^2 k^6]/\Sigma[(\chi_{obsd})^2 k^6]$. MS = multiple scattering. The S_0^2 factor was set at 1.

Component	N	R(Å)	σ^2 (Å^2)
Fe-O/N	6	2.11	932
Fe-C	2	2.93	245
Fe-C	5	3.20	624
C-O MS	10	3.22	619
C-N MS	10	4.30	947
C-O MS	4	4.47	580
C-C MS	2	5.02	702
		E_0 = -6.42	
		Error = 20.43	

Table S7: Full fit parameters for (Fe$^{\mathrm{II}}$/αKG/penG)-DAOCS. σ^2 values are multiplied by 10^5. E_0 is the energy shift from 7130 eV to give the experimental ionization energy of the 1s electron. The error value is the weighted F-factor given by the statistical F test used to evaluate EXAFS fits. Error is given by $\Sigma[(\chi_{obsd} - \chi_{calc})^2 k^6]/\Sigma[(\chi_{obsd})^2 k^6]$. MS = multiple scattering. The S_0^2 factor was set at 1.

2.2 Reaction of five- and six-coordinate (Fe^{II}/αKG)-DAOCS with O_2

Upon the reaction of Fe^{II}/αKG)-DAOCS with O_2, there are features that appear between $\pm 4 - 8$ mm/s (Fig. S9). The final reacted spectrum (Fig. S10, black) contains two Fe(III) species. One of the species is the active site Fe(III) species that has been fit with the parameters in figure 2. The second species ($< 15\%$ of the total integrated area of the 18 second spectrum) has a six-line hyperfine pattern (indicated by the red asterisks) that results from uncoupled turnover during the rapid freeze quench procedure and is no longer active. This was determined by the addition of αKG and penG, which reduce the Fe(III)-DAOCS active site to Fe(II)-DAOCS with no change in these hyperfine features (see SI sections 2.3.2 and 2.3.3).

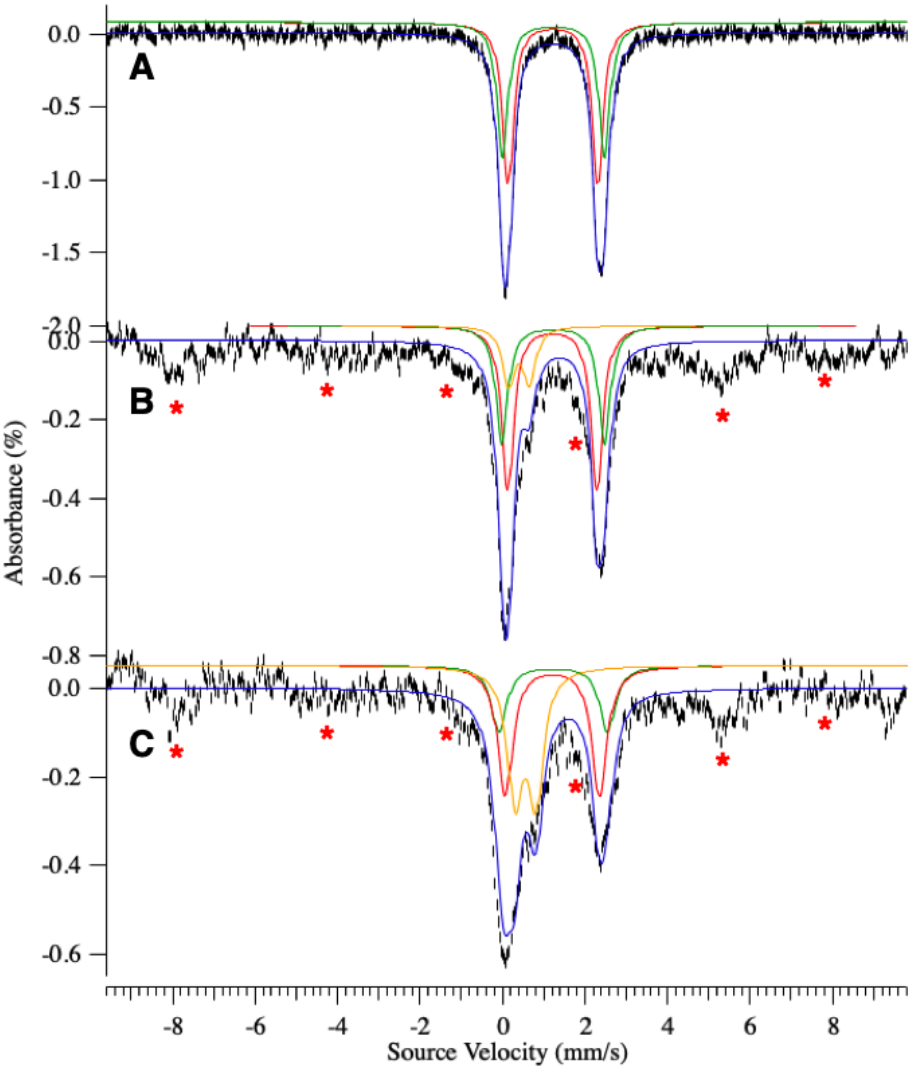

Figure S9: Zero field Mössbauer collected at 6 K A) (Fe^{II}/αKG)-DAOCS B) (Fe^{II}/αKG)-DAOCS reacted with 1 equivalent of O_2 (at 4°C) and freeze quenched at 6 s and C) 18 s (Note: same data as Fig. 2 with full source velocity range). The red asterisks indicate the presence of irreversible Fe(III) formed during uncoupled turnover.

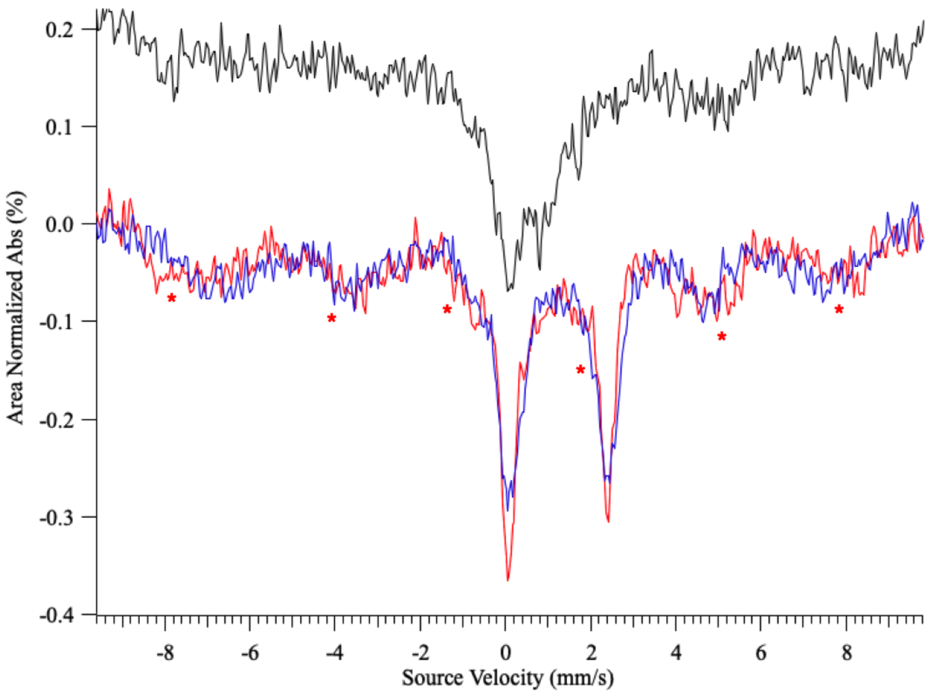

Figure S10: Zero field Mössbauer collected at 6 K of *(top)* ($Fe^{II}/\alpha KG$)-DAOCS reacted with 1 equivalent O_2 (at 4°C) freeze quenched at 600 s (black) and *(bottom)* the final spectrum upon further reaction with either αKG (red) or penG (blue). The red asterisks indicate the presence of irreversible Fe(III) formed during uncoupled turnover.

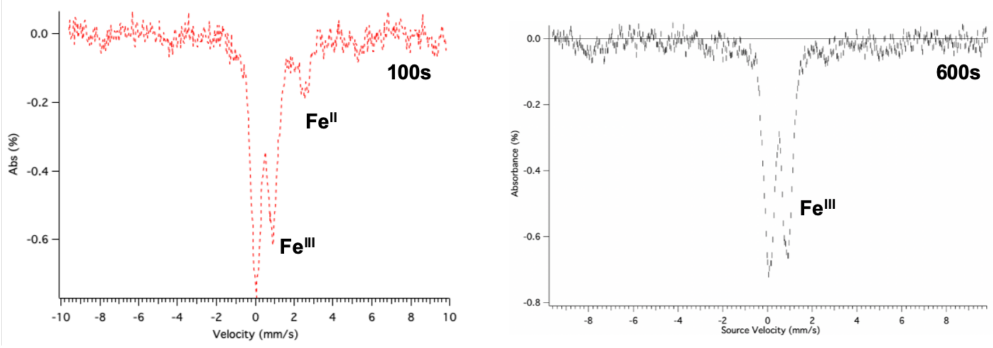

Figure S11: Zero field Mössbauer collected at 50 K of ($Fe^{II}/\alpha KG$)-DAOCS reacted with 1 equivalent O_2 (at 4°C) freeze quenched at 100s (left, red) and 10 minutes (right, black). In the 100s Mössbauer spectrum (red, left), the Fe(II) doublet is ∼10-15%.

A kinetic model was built (Fig. S12A) that captures the biphasic growth of the 335nm and 380nm absorption time traces (Fig. 3A) along with the change in the relative five- and six-coordinate ratios during the O_2 reaction from Mössbauer spectroscopy (Fig. 2, S9, S10 and S11). From Fig. S4 and Table S1, the equilibrium ratio of the five- and six-coordinate components in the αKG bound Fe^{II}-DAOCS sample yields a $K_{eq} = 0.83$, which defines the ratio between k_1 and k_{-1} in Fig. S11A. Fitting the kinetic model to the experimental 380nm time trace (Fig. S12B) yield rate constants (Fig. S12A) that simulate the relative ratios of five- and six-coordiante Fe(II) and Fe(III) in agreement with the experimental Mössbauer spectra (Fig. S12C and D).

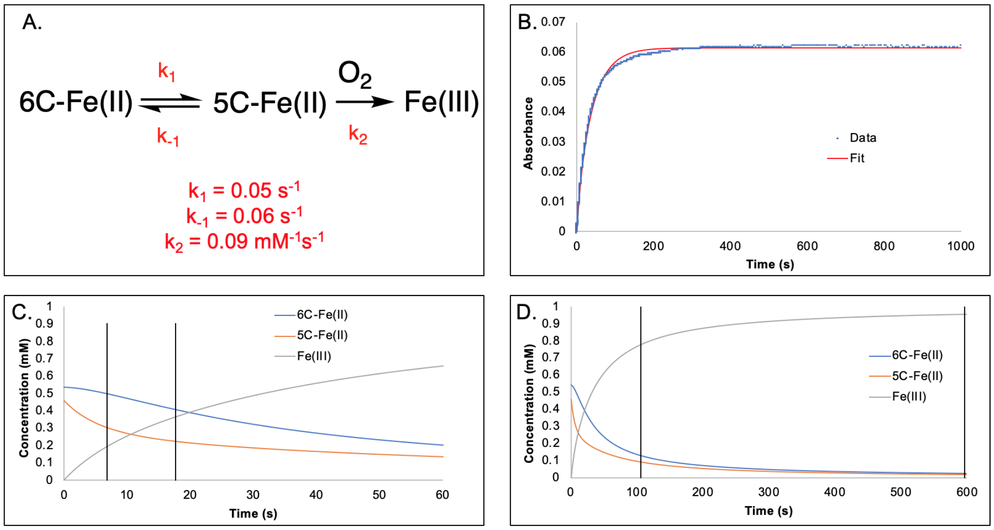

Figure S12: A) Kinetic model for the reaction of (Fe^{II}/αKG)-DAOCS with O_2. B) Fit (red) to the time trace monitored at 380 nm during the reaction of 0.1 mM (Fe^{II}/αKG)-DAOCS with 1 mM O_2. C,D) Simulation of kinetic model presented in A) with the Mössbauer reaction conditions of 1 mM (Fe^{II}/αKG)-DAOCS with 1 mM O_2. The relative five-coordinate (5C) and six-coordinate (6C) species concentrations obtained from the simulations are shown with the black vertical lines and agree with the speciation obtained from Mössbauer spectroscopy (Fig. 2, S9 and S11).

2.3 Characterization of the Fe^{III} Species and its Reactivity: Evaluation of the Sequential Mechanism

2.3.1 Definition of the Fe^{III} Species obtained from Reaction of (Fe^{II}/αKG)-DAOCS with O_2

In Fig. S13, the autooxidized Fe(III)-DAOCS site (black) does not reproduce the 335nm and 380nm absorption features observed in the Fe^{III} species generated from the reaction of (Fe^{II}/αKG)-DAOCS with O_2 (green). However, upon binding of succinate to Fe^{III}-DAOCS, the 335nm and 380nm features (red traces) grow in. In order to evaluate the origin of this absorption intensity in Fig. S13 that arises from succinate binding (red trace relative to black trace), two computational models were assessed. Octahedral models of Fe^{III}-OH with 2 histidines (His), 1 carboxylate with either a bound bidentate succinate (Fig. S14B) or 2 waters (Fig. S14A) were constructed. These structures were optimized using a hybrid functional that incorporates long-range correction, CAM-B3LYP, in Gaussian 09 with solvation effects included using a polarized continuum model with a dielectric constant $\epsilon = 4.0$.[21] Comparing the optimized structures (Fig. S13), the Fe-OH bond elongates from 1.82Å to 1.87Å upon succinate binding. When absorption spectra of these two models were simulated using time-dependent density functional theory (TD-DFT, Fig. S15), the charge transfer (CT) from the out-of-plane hydroxy π orbital to the Fe^{III} d_{xz} orbital shifts from 30,700 cm^{-1} to 24,500 cm^{-1} when succinate is bound. Since the Fe-OH bond elongates by 0.05Å upon succinate binding (Fig. S14), this decrease in energy of the OH-to-Fe^{III} CT is due to diminished interaction between the hydroxide and iron causing the bond/antibonding combination of these two π orbitals to be closer in energy. Thus, the absorption feature corresponding to the CT transition between these orbitals appears at lower energy when succinate is bound to the Fe(III)-DAOCS autooxidized site (red vs black traces in Fig. S13).

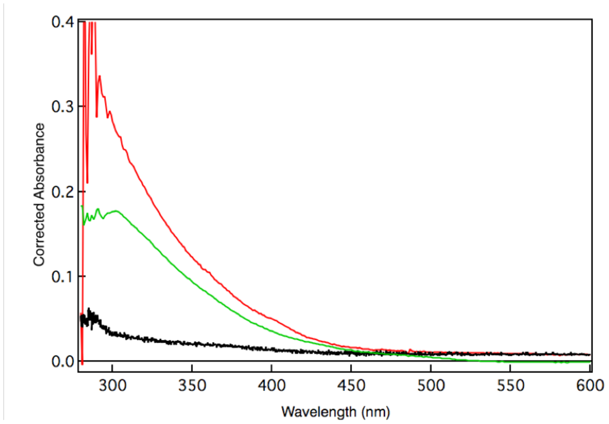

Figure S13: Room temperature UV-Vis spectra of Fe^{III}-DAOCS obtained by auto-oxidation in O_2 for two hours (black), (Fe^{III}/succinate)-DAOCS (red) and the 335/380 nm species (green). The Fe^{II} protein background signal was subtracted, and spectra were corrected for the amount of Fe^{III}. These spectra show that the 335/380 nm features observed in Figure 3 arise from a succinate-bound Fe^{III} species.

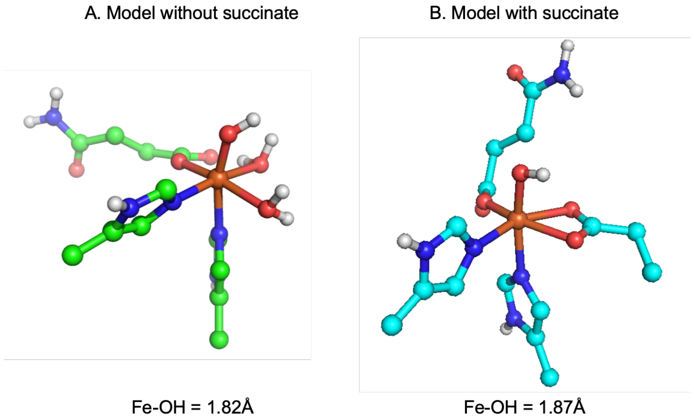

Figure S14: Geometry optimized $\mathrm{Fe^{III}}$-OH models without (A) and with (B) succinate bound to the iron center. Upon succinate binding, the Fe-OH bond elongates by 0.05Å

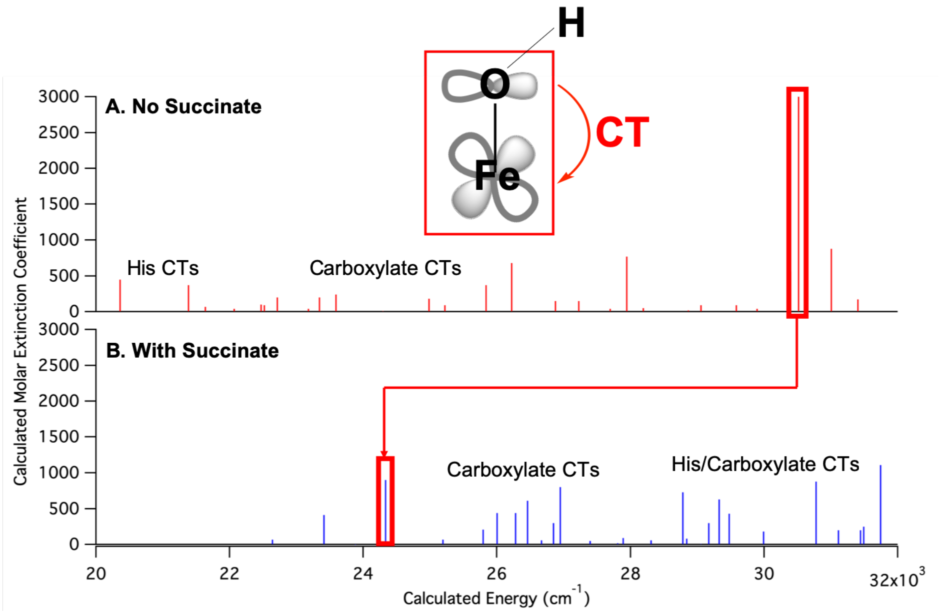

Figure S15: TD-DFT absorption spectra for $\mathrm{Fe^{III}}$-OH complexes without (top, red sticks) and with (bottom, blue sticks) succinate bound to the metal center. The red boxes indicate the energies of the out-of-plane OH-to-$\mathrm{Fe^{III}}$ CT (inset) and the observed shift upon succinate binding.

2.3.2 Reduction of Fe^{III}(OH)(Succinate) Species by αKG: Ability to perform multiple turnovers

Upon generation of the Fe^{III}(OH)(Succinate) species, its reactivity with excess αKG was evaluated. A double mix experiment was performed where the Fe^{III} species was first generated by mixing (Fe^{II}/αKG)-DAOCS (with 1 eq. αKG) with O_2 and this Fe^{III} was then mixed with 10 addition equivalents of αKG. Upon addition of the excess αKG, the 335/380nm features decay (Fig. S16) and the Fe^{III} species converts to an Fe^{II} species (Fig. S17). The additional αKG in solution reduces the Fe^{III} site to a viable Fe^{II} active site, which can undergo multiple turnover with additional equivalents of O_2 and αKG (Fig. S18 and S19).

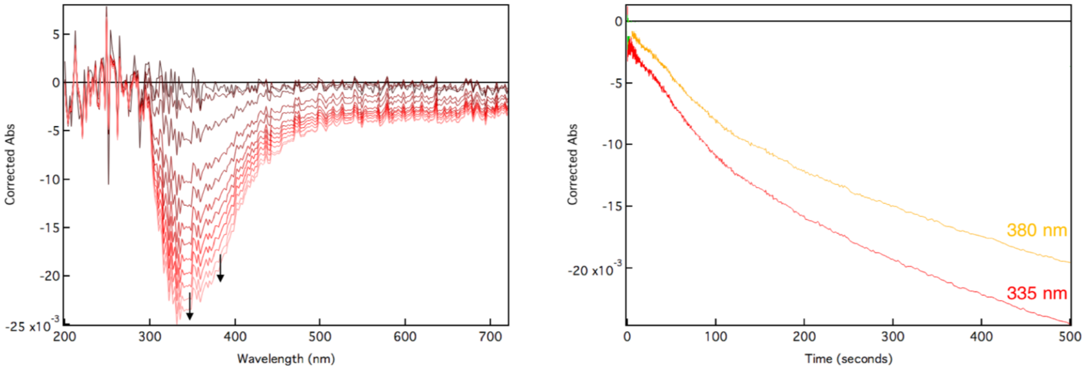

Figure S16: *(Left)* UV-Vis absorption difference spectra (collected at 5°C) monitoring the reaction between the Fe^{III}(OH)(Succinate) species (0.2 mM) and 10 additional equivalents of αKG (2 mM). *(Right)* Kinetic traces from the same experiment showing decreasing absorbances at 335 nm (red) and 380 nm (yellow).

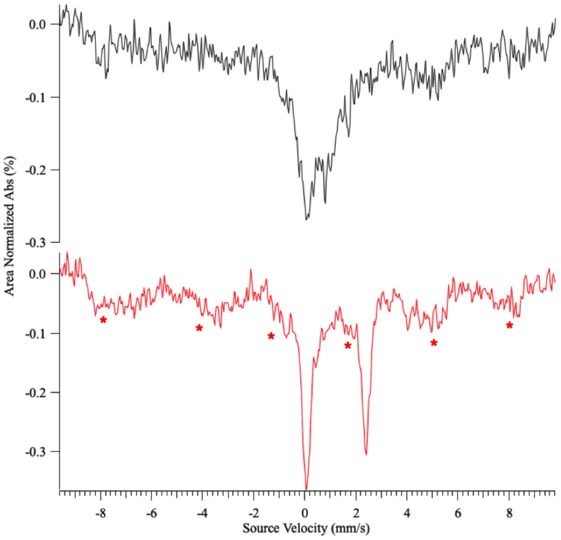

Figure S17: Mössbauer spectra of the Fe^{III}(OH)(Succinate) species (collected at 0 T and 6 K, black, *top*) and the αKG reacted species (red, *bottom*). The Fe^{III}(OH)(Succinate) species was pre-formed and then mixed with 10x αKG. Concomitant with the decay of the 335 and 380 nm features (Fig. S16), the Mössbauer data show a conversion of high-spin Fe^{III} (δ = 0.43 mm/s) to high-spin Fe^{II} (δ = 1.23 mm/s). Red asterisks indicate irreversible Fe^{III} remaining after reaction with PenG, see text above Figure S9 and Figure S9 for full explanation.

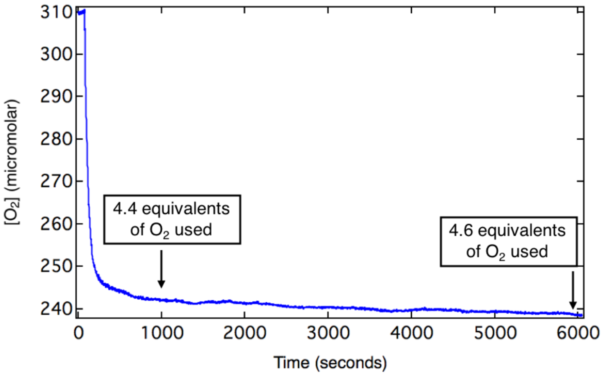

Figure S18: Concentration of O_2 in oxygenated buffer solution monitored by a Clark electrode before and after addition of concentrated (Fe^{II}/αKG)-DAOCS. The concentrated (Fe^{II}/αKG)-DAOCS has a 10-fold excess of αKG relative to DAOCS. UV/Vis and Mössbauer data (Figure S16 and S17) showed that excess αKG in solution can reduce the 335/380 nm species to Fe^{II}, and this oxygen consumption assay shows that upon reduction of the active site Fe, DAOCS can react with O_2 for multiple turnovers.

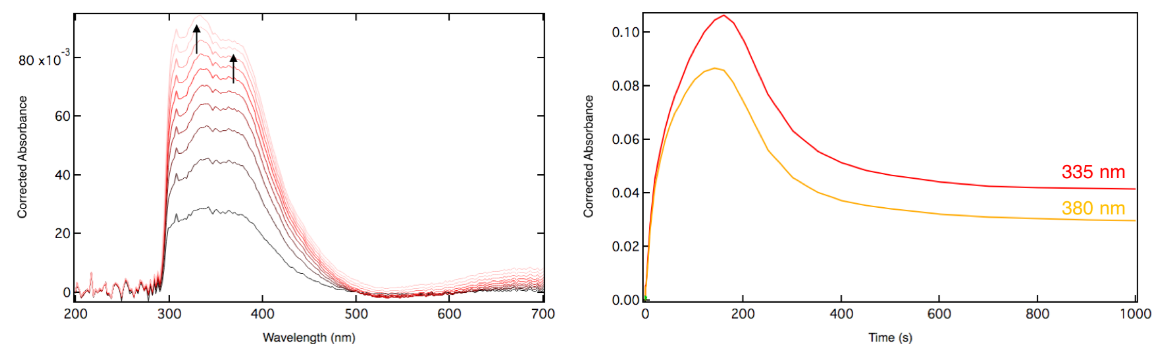

Figure S19: UV-vis absorption spectra collected at 5°C after equal volume mixing of a solution of 0.2 mM DAOCS, 0.2 mM Fe^{II} and 1 mM αKG in 50 mM HEPES, pH 7.5 with O_2-saturated buffer and with the spectrum of the mix with O_2-free buffer subtracted (left). Kinetic traces from the same experiment showing absorbances at 335 nm (red) and 380 nm (yellow). In the absence of substrate and presence of excess αKG, DAOCS can turnover multiple times to generate a high-spin Fe^{III} species (with 335 and 380 nm features) that can be reduced by excess αKG to re-enter the cycle. With only one equivalent of αKG, the 335/380 nm features are stable over hours. The incomplete decay of the 335/380 nm features observed in the absorption experiment in the presence of excess αKG is due to a combination of multiple turnovers and the generation of a stable species once the αKG has been used up.

2.3.3 Reaction of Fe^{III}(OH)(Succinate) with penG: Inability to Produce Cephalosporin Product

The reaction of the Fe^{III}(OH)(Succinate) species (produced from the reaction of (Fe^{II}/αKG) with O$_2$) with penG was assessed. A double mix experiment was performed where the Fe^{III} species was first generated and allowed to fully oxidize and then mixed with penG substrate. Upon addition of substrate, the 335/380nm features decay (Fig. S20) and the Fe^{III} species converts to an Fe^{II} species (Fig. S21). The substrate oxidizes by one electron to an EPR active sulfur radical species that has a g $\sim$ 2.08. (Fig. S22) and does not produce cephalosporin product.

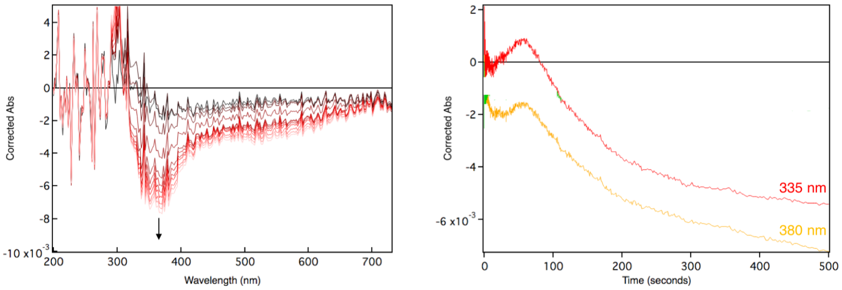

Figure S20: UV-Vis absorption difference spectra (collected at 5°C) monitoring the reaction between the Fe^{III}(OH)(Succinate) species (0.2 mM) with 1 additional equivalent of penG (0.2 mM) (left). Kinetic traces from the same experiment showing absorbances at 335 nm (red) and 380 nm (yellow) (right). The increase at $\sim$70 seconds in the 335 and 380 nm kinetic traces is due to the absorbance of the penicillin substrate.

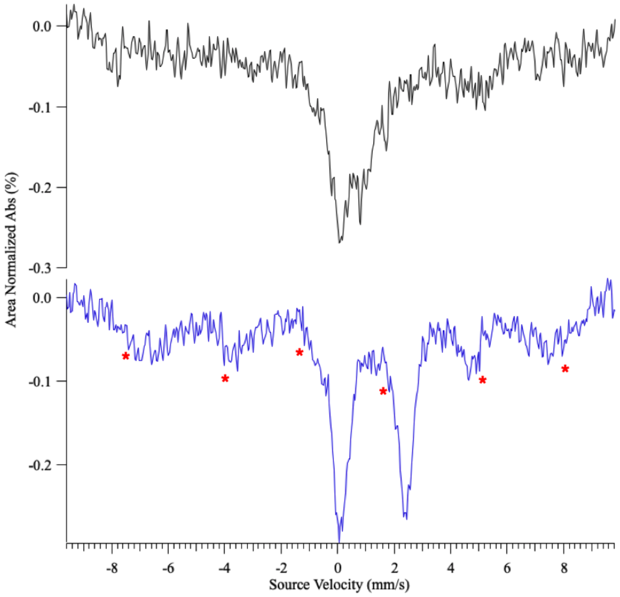

Figure S21: Mössbauer spectra of the Fe^{III}(OH)(Succinate) species (collected at 0 T and 6 K, black, *top*) and the penG reacted species (blue, *bottom*). The Fe^{III}(OH)(Succinate) species was pre-formed and then mixed with 30x penG. Concomitant with the decay of the 335 and 380 nm features (Fig. S16), the Mössbauer data show a conversion of high-spin Fe^{III} (δ = 0.43 mm/s) to high-spin Fe^{II} (δ = 1.24 mm/s). Red asterisks indicate irreversible Fe^{III} remaining after reaction with PenG, see text above Figure S9 and Figure S9 for full explanation.

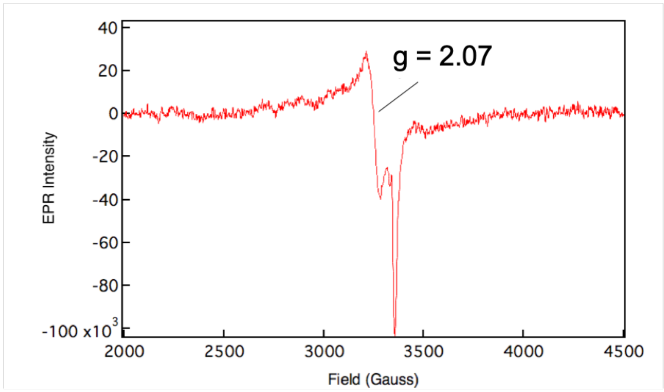
A. EPR Spectrum of oxidized penG

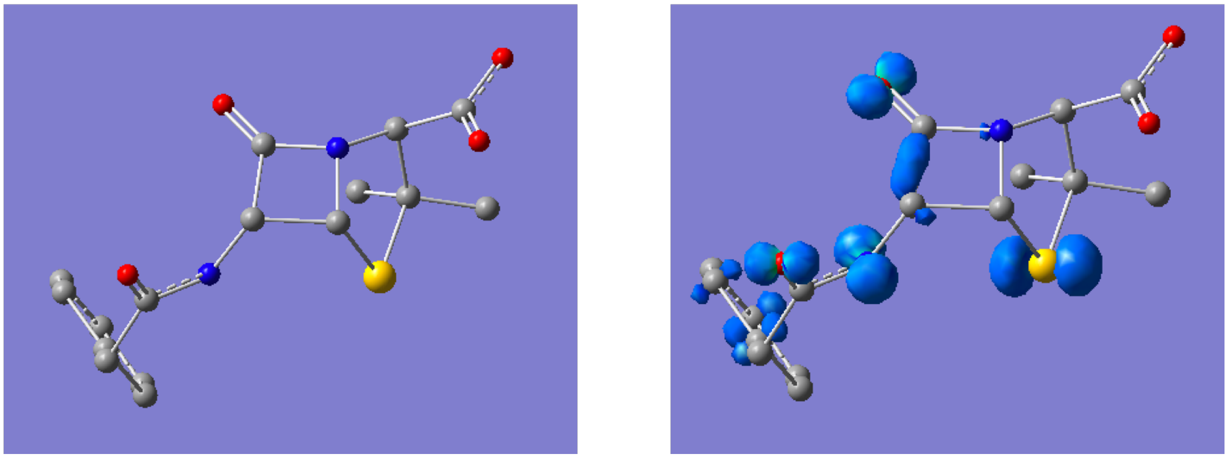
B. Geometry Optimized Structure of oxidized penG

C. Visualization of spin density on oxidized penG

Figure S22: A) 77 K X-band EPR spectrum of (Fe^{II}/αKG)-DAOCS with one equivalent of αKG bound and rapidly mixed with excess O$_2$, then mixed with 30 equivalents of penG. The g value >2.02 is indicative of a sulfur-based radical and suggests that penG has been oxidized by one electron. The reduction of Fe^{III} to Fe^{II} by penG in the same experiment monitored by Mössbauer (Fig. S21) supports this. B) Electronic structure calculations were performed on the 1-electron oxidized penG substrate. This radical was geometry optimized using the BP86 functional and a 6-311G* basis set. C) The calculation of oxidized penG shows 30% of the electron spin density on the sulfur atom of the penicillin ring. This sulfur radical is similar to other sulfur-based radicals in the literature.[30,31]

2.4 Reactivity of (Fe^{II}/αKG/penG)-DAOCS site with O_2 - Coupled Turnover via the Concerted Mechanism

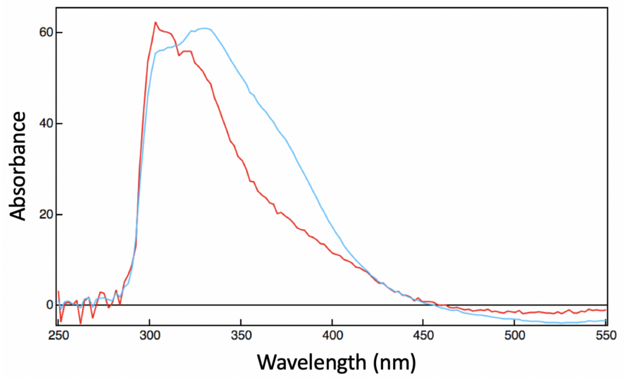

Figure S23: UV-vis absorption spectra collected at 5 °C after equal volume mixing of a solution of 0.26 mM DAOCS, 0.26 mM Fe^{II}, 8 mM penG and 0.26 mM αKG in 50 mM HEPES, pH 7.5 with O_2-saturated buffer (2 mM), with the spectrum of DAOCS/αKG/penG mixed with O_2-free buffer subtracted at 2 s (red, scaled) and 25 s (blue).

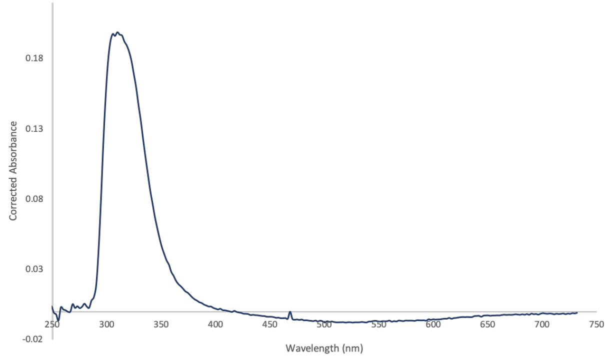

Figure S24: UV-Vis absorbance spectrum collected at 30 minutes and 5°C after equal volume mixing of a solution of 0.26 mM DAOCS, 0.26 mM Fe^{II}, 8 mM penG and 0.26 mM αKG in 50 mM HEPES, pH 7.5 with 0.2 mM O_2 in buffer and with the spectrum of the mix with O_2-free buffer subtracted. This is the spectrum of the cephalosporin product of DAOCS penicillin G ring expansion.[32]

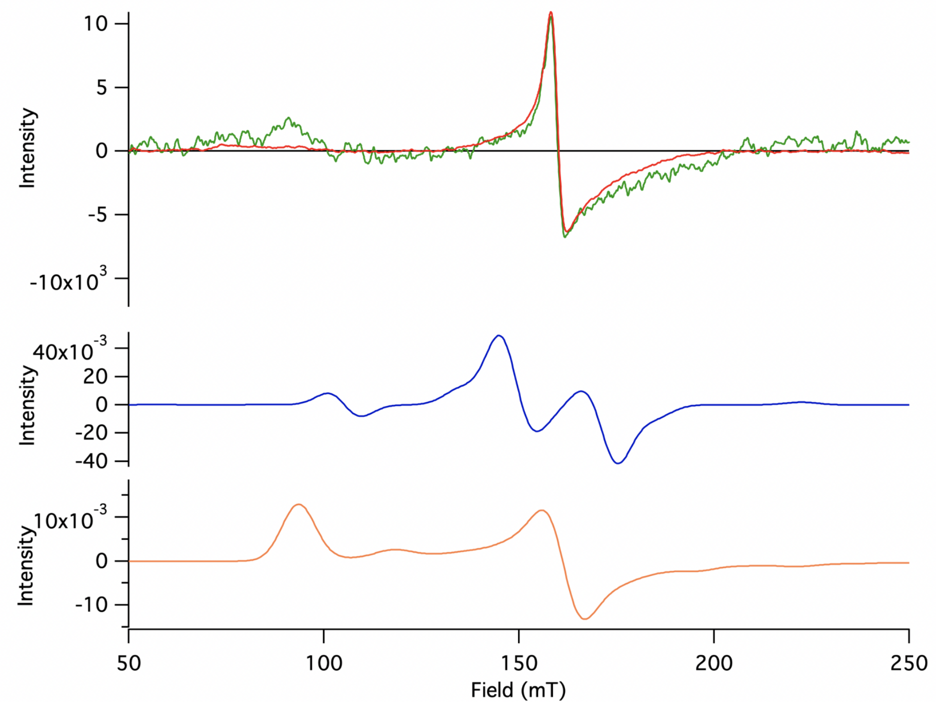

Figure S25: The overlay of the 5K and 50 μW EPR spectra of the (Fe^{II}/αKG)-DAOCS + O_2 (red) and (Fe^{II}/αKG/penG)-DAOCS + O_2 (green) reactions reveal a new feature at 900mT or g' ∼ 7.5. This feature grows and decays with the g' ∼ 4.3 and g ∼ 2.0 EPR signals (i.e. the g' ∼ 7.5 signal also decays as the product is formed). Three approaches were evaluated to fit the g' ∼ 7.5 feature. 1) The Fe^{III} and g ∼ 2 spins were dipolar coupled at different distances from each other. At ∼4Å, the simulation features a g' ∼ 7.5 signal with reasonable intensity in the g' ∼ 4.3 region (blue spectrum). 2) The Fe^{III} signal was made axial with an E/D value of 0.07, which corresponds to the simulation in orange and match the two resonances at g' ∼ 7.5 and g' ∼ 4.3 for the Fe^{III} ion. 3) Exchange coupling the g' ∼ 4.3 and g ∼ 2 radicals, which did not give a simulation consistent with the experimental spectrum. Based on spin quantitation, the g' ∼ 4.3 and g ∼ 2 signals account for 70-80% of total concentration and the g' ∼ 7.5 accounts for 20-30%. Thus, the g' ∼ 7.5 signal can either reflect a 20% component that has a more axial Fe^{III} site or 20% of the Fe^{III}-OH site that dipolar couples to the radical.

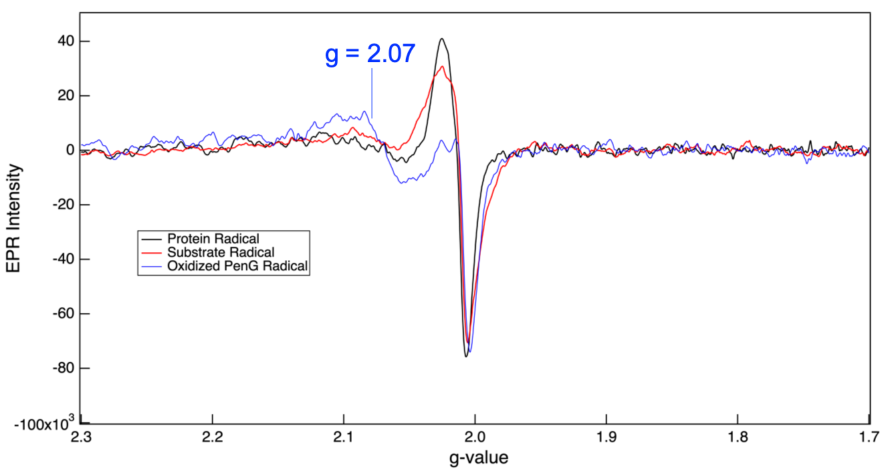

Figure S26: Overlay of the protein radical (black) produced in the reaction of Fe^{II}/αKG with O_2 (Fig. 3B), substrate radical (red) produced in the reaction of Fe^{II}/αKG/penG with O_2 (Fig. 4E) and the oxidized penicillin-G radical (blue) produced in the reaction of Fe^{III}(OH)(succinate) with penG (Fig. S22). The sulfur radical (blue) is similar to other sulfur-based radicals in the literature.[30,31]

Reactant	Product	ΔH (kcal/mol)
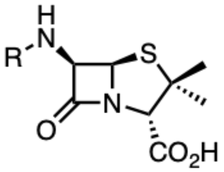	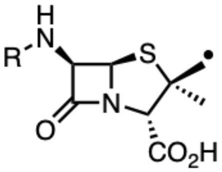	99.3
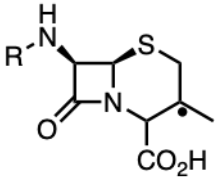	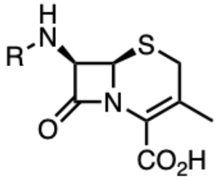	35.9

Table S8: DFT calculated bond dissociation enthalpies for C-H bond breaking in ring expansion of penG catalyzed by DAOCS. Structures of penicillin G, penicillin G with a β-methylene radical, ring-expanded tertiary carbon radical and cephalosporin product were geometry optimized using the BP86 functional with 10% Hartree-Fock exchange and a 6-311G* basis set.

References

[1] Source: SSRL Biological XAS beam line 7-3, -. p., 2-T wiggler, 0.8 mrad beam, SPEAR3 at 3 GeV. Optics: Si(220), liquid nitrogen cooled double crystal monochromator, fully tuned. Premonochromator flat, bent, vertically collimating Rh-coated Si M0 mirror; 9.5 keV cutoff, energy resolution 1x10^{-4} ΔE/E.

[2] Source: SSRL Biological XAS beam line 9-3, -. p., 2-T wiggler, 2.0 mrad beam, SPEAR3 at 3 GeV. Optics: Si(220), liquid nitrogen cooled double crystal monochromator, fully tuned. Premonochromator flat, bent, vertically collimating Rh-coated Si M0 mirror; and post-30 monochromator bent, cylindrical, Rh-coated Si focusing M1 mirror; 10 keV cutoff, energy resolution 1x10^{-4} ΔE/E.

[3] S P Cramer, O Tench, M Yocum, and George G N. *Accelerators, Spectrometers, Detectors and Associated Equipment*, volume 266. 1988.

[4] Robert A. Scott, James E. Hahn, Sebastian Doniach, Hans C. Freeman, and Keith O. Hodgson. Polarized x-ray absorption spectra of oriented plastocyanin single crystals. investigation of methionine-copper coordination. *Journal of the American Chemical Society*, 104(20):5364–5369, 1982.

[5] Robert A Scott. [23] measurement of metal-ligand distances by exafs. In *Methods in enzymology*, volume 117, pages 414–459. Elsevier, 1985.

[6] Jane G DeWitt, James G Bentsen, Amy C Rosenzweig, Britt Hedman, Jeffrey Green, Simon Pilkington, Georgia C Papaefthymiou, Howard Dalton, Keith O Hodgson, and Stephen J Lippard. X-ray absorption, mössbauer, and epr studies of the dinuclear iron center in the hydroxylase component of methane monooxygenase. *Journal of the American Chemical Society*, 113(24):9219–9235, 1991.

[7] Stephen P Cramer and Keith O Hodgson. X-ray absorption spectroscopy: a new structural method and its applications to bioinorganic chemistry. *Progress in inorganic chemistry*, 25:1–39, 1979.

[8] Adam Tenderholt, Britt Hedman, and Keith O Hodgson. Pyspline: A modern, cross-platform program for the processing of raw averaged xas edge and exafs data. In *AIP conference Proceedings*, volume 882, pages 105–107. AIP, 2007.

[9] Tami E Westre, Pierre Kennepohl, Jane G DeWitt, Britt Hedman, Keith O Hodgson, and Edward I Solomon. A multiplet analysis of fe k-edge 1s - 3d pre-edge features of iron complexes. *Journal of the American Chemical Society*, 119(27):6297–6314, 1997.

[10] George, G. N.; Pickering, I. J. EDG_FIT, Stanford Synchrotron Radiation Laboratory, Stanford Linear Accelerator Center, Stanford University, Stanford, CA., 2000.

[11] George, G. N.; Pickering, I. J. EXAFSPAK, Stanford Synchrotron Radiation Laboratory, Stanford Linear Accelerator Center, Stanford University, Stanford, CA., 2000.

[12] George, G. N.; Pickering, I. J. OPT, Stanford Synchrotron Radiation Laboratory, Stanford Linear Accelerator Center, Stanford University, Stanford, CA., 2000.

[13] A Michalowicz, K Provost, S Laruelle, A Mimouni, and G Vlaic. F-test in exafs fitting of structural models. *Journal of synchrotron radiation*, 6(3):233–235, 1999.

[14] Stephen P Cramer, Keith O Hodgson, Edward I Stiefel, and William E Newton. A systematic x-ray absorption study of molybdenum complexes. the accuracy of structural information from extended x-ray absorption fine structure. *Journal of the American Chemical Society*, 100(9):2748–2761, 1978.

[15] Karin Valegård, Anke C Terwisscha Van Scheltinga, Matthew D Lloyd, Takane Hara, S Ramaswamy, Anastassis Perrakis, Andy Thompson, Hwei-Jen Lee, Jack E Baldwin, Christopher J Schofield, et al. Structure of a cephalosporin synthase. *Nature*, 394(6695):805, 1998.

[16] Karin Valegård, Anke C Terwisscha van Scheltinga, Alain Dubus, Graziella Ranghino, Linda M Öster, Janos Hajdu, and Inger Andersson. The structural basis of cephalosporin formation in a mononuclear ferrous enzyme. *Nature structural & molecular biology*, 11(1):95, 2004.

[17] Stefan Hoops, Sven Sahle, Ralph Gauges, Christine Lee, Jürgen Pahle, Natalia Simus, Mudita Singhal, Liang Xu, Pedro Mendes, and Ursula Kummer. Copasi—a complex pathway simulator. *Bioinformatics*, 22(24):3067–3074, 2006.

[18] M. J. Frisch, G. W. Trucks, H. B. Schlegel, G. E. Scuseria, M. A. Robb, J. R. Cheeseman, G. Scalmani, V. Barone, B. Mennucci, G. A. Petersson, H. Nakatsuji, M. Caricato, X. Li, H. P. Hratchian, A. F. Izmaylov, J. Bloino, G. Zheng, J. L. Sonnenberg, M. Hada, M. Ehara, K. Toyota, R. Fukuda, J. Hasegawa, M. Ishida, T. Nakajima, Y. Honda, O. Kitao, H. Nakai, T. Vreven, J. A. Montgomery, Jr., J. E. Peralta, F. Ogliaro, M. Bearpark, J. J. Heyd, E. Brothers, K. N. Kudin, V. N. Staroverov, R. Kobayashi, J. Normand, K. Raghavachari, A. Rendell, J. C. Burant, S. S. Iyengar, J. Tomasi, M. Cossi, N. Rega, J. M. Millam, M. Klene, J. E. Knox, J. B. Cross, V. Bakken, C. Adamo, J. Jaramillo, R. Gomperts, R. E. Stratmann, O. Yazyev, A. J. Austin, R. Cammi, C. Pomelli, J. W. Ochterski, R. L. Martin, K. Morokuma, V. G. Zakrzewski, G. A. Voth, P. Salvador, J. J. Dannenberg, S. Dapprich, A. D. Daniels, Ö. Farkas, J. B. Foresman, J. V. Ortiz, J. Cioslowski, and D. J. Fox. Gaussian?09 Revision E.01. Gaussian Inc. Wallingford CT 2009.

[19] Axel D Becke. Density-functional exchange-energy approximation with correct asymptotic behavior. *Physical review A*, 38(6):3098, 1988.

[20] Christopher J Cramer and Donald G Truhlar. Implicit solvation models: equilibria, structure, spectra, and dynamics. *Chemical Reviews*, 99(8):2161–2200, 1999.

[21] T. Yanai, D.P. Tew, and N.C. Handy. A new hybrid exchange-correlation functional using the coulomb-attenuating method (cam-b3lyp). *Chemical Physics Letters*, 393:51–57, 2004.

[22] Edward I Solomon, Elizabeth G Pavel, Kelly E Loeb, and Cecelia Campochiaro. Magnetic circular dichroism spectroscopy as a probe of the geometric and electronic structure of non-heme ferrous enzymes. *Coordination chemistry reviews*, 144:369–460, 1995.

[23] Edward I Solomon, Thomas C Brunold, Mindy I Davis, Jyllian N Kemsley, Sang-Kyu Lee, Nicolai Lehnert, Frank Neese, Andrew J Skulan, Yi-Shan Yang, and Jing Zhou. Geometric and electronic structure/function correlations in non-heme iron enzymes. *Chemical reviews*, 100(1):235–350, 2000.

[24] Kenneth M Light, John A Hangasky, Michael J Knapp, and Edward I Solomon. Spectroscopic studies of the mononuclear non-heme feii enzyme fih: Second-sphere contributions to reactivity. *Journal of the American Chemical Society*, 135(26):9665–9674, 2013.

[25] Elizabeth G Pavel, Jing Zhou, Robert W Busby, Michele Gunsior, Craig A Townsend, and Edward I Solomon. Circular dichroism and magnetic circular dichroism spectroscopic studies of the non-heme ferrous active site in clavaminate synthase and its interaction with α-ketoglutarate cosubstrate. *Journal of the American Chemical Society*, 120(4):743–753, 1998.

[26] Mindy I Davis, Erik C Wasinger, Andrea Decker, Monita YM Pau, Frédéric H Vaillancourt, Jeffrey T Bolin, Lindsay D Eltis, Britt Hedman, Keith O Hodgson, and Edward I Solomon. Spectroscopic and electronic structure studies of 2, 3-dihydroxybiphenyl 1, 2-dioxygenase: O2 reactivity of the non-heme ferrous site in extradiol dioxygenases. *Journal of the American Chemical Society*, 125(37):11214–11227, 2003.

[27] DM Arciero, JD Lipscomb, BH Huynh, TA Kent, and E Münck. Epr and mössbauer studies of protocatechuate 4, 5-dioxygenase. characterization of a new fe2+ environment. *Journal of Biological Chemistry*, 258(24):14981–14991, 1983.

[28] Marina S Chow, Bekir E Eser, Samuel A Wilson, Keith O Hodgson, Britt Hedman, Paul F Fitzpatrick, and Edward I Solomon. Spectroscopy and kinetics of wild-type and mutant tyrosine hydroxylase: Mechanistic insight into o2 activation. *Journal of the American Chemical Society*, 131(22):7685–7698, 2009.

[29] A. Michalowicz, K. Provost, S. Laruelle, A. Mimouni, and G. Vlasic. F-test in exafs fitting of structural models. *Journal of Synchrotron Radiation*, 6(3):233–235, 1999.

[30] A.L. Persson, M. Sahlin, and B. Sjöberg. Cysteinyl and substrate radical formation in active site mutant e441q of *Escherichia coli* class i ribonucleotide reductase. *Journal of Biological Chemistry*, 273(47):31016–31020, 1998.

[31] S. Licht, G.J. Gerfen, and J. Stubbe. Thiyl radicals in ribonucleotide reductases. *Science*, 271:477–481, 1996.

[32] Dubus A., M.D. Lloyd, H.-J. Lee, C.J. Schofield, J.E. Baldwin, and J.-M. Frere. Probing the penicillin sidechain selectivity of recombinant deacetoxycephalosporin c synthase. *Cellular and Molecular Life Sciences*, 58:835–843, 2001.